



Fermi National Accelerator Laboratory

FERMILAB-Pub-95/033-E

CDF

Measurement of the W Boson Mass

F. Abe et al.
The CDF Collaboration
Fermi National Accelerator Laboratory
P.O. Box 500, Batavia, Illinois 60510

March 1995

Submitted to *Physical Review D*

Disclaimer

This report was prepared as an account of work sponsored by an agency of the United States Government. Neither the United States Government nor any agency thereof, nor any of their employees, makes any warranty, express or implied, or assumes any legal liability or responsibility for the accuracy, completeness, or usefulness of any information, apparatus, product, or process disclosed, or represents that its use would not infringe privately owned rights. Reference herein to any specific commercial product, process, or service by trade name, trademark, manufacturer, or otherwise, does not necessarily constitute or imply its endorsement, recommendation, or favoring by the United States Government or any agency thereof. The views and opinions of authors expressed herein do not necessarily state or reflect those of the United States Government or any agency thereof.

Measurement of the W Boson Mass

F. Abe,¹³ M. G. Albrow,⁷ D. Amidei,¹⁶ J. Antos,²⁸ C. Anway-Wiese,⁴
 G. Apollinari,²⁶ H. Areti,⁷ M. Atac,⁷ P. Auchincloss,²⁵ F. Azfar,²¹ P. Azzi,²⁰
 N. Bacchetta,¹⁸ W. Badgett,¹⁶ M. W. Bailey,¹⁸ J. Bao,³⁴ P. de Barbaro,²⁵
 A. Barbaro-Galtieri,¹⁴ V. E. Barnes,²⁴ B. A. Barnett,¹² P. Bartalini,²³
 G. Bauer,¹⁵ T. Baumann,⁹ F. Bedeschi,²³ S. Behrends,³ S. Belforte,²³
 G. Bellettini,²³ J. Bellinger,³³ D. Benjamin,³² J. Benlloch,¹⁵ J. Bensinger,³
 D. Benton,²¹ A. Beretvas,⁷ J. P. Berge,⁷ S. Bertolucci,⁸ A. Bhatti,²⁶
 K. Biery,¹¹ M. Binkley,⁷ F. Bird,²⁹ D. Bisello,²⁰ R. E. Blair,¹ C. Blocker,²⁹
 A. Bodek,²⁵ W. Bokhari,¹⁵ V. Bolognesi,²³ D. Bortoletto,²⁴ C. Boswell,¹²
 T. Boulos,¹⁴ G. Brandenburg,⁹ C. Bromberg,¹⁷ E. Buckley-Geer,⁷ H. S. Budd,²⁵
 K. Burkett,¹⁶ G. Busetto,²⁰ A. Byon-Wagner,⁷ K. L. Byrum,¹ J. Cammerata,¹²
 C. Campagnari,⁷ M. Campbell,¹⁶ A. Caner,⁷ W. Carithers,¹⁴ D. Carlsmith,³³
 A. Castro,²⁰ Y. Cen,²¹ F. Cervelli,²³ H. Y. Chao,²⁸ J. Chapman,¹⁶ M.-
 T. Cheng,²⁸ G. Chiarelli,⁸ T. Chikamatsu,³¹ C. N. Chiou,²⁸ S. Cihangir,⁷
 A. G. Clark,²³ M. Cobal,²³ M. Contreras,⁵ J. Conway,²⁷ J. Cooper,⁷
 M. Cordelli,⁸ D. Crane,¹ J. D. Cunningham,³ T. Daniels,¹⁵ F. DeJongh,⁷
 S. Delchamps,⁷ S. Dell'Agnello,²³ M. Dell'Orso,²³ L. Demortier,²⁶ B. Denby,²³
 M. Deninno,² P. F. Derwent,¹⁶ T. Devlin,²⁷ M. Dickson,²⁵ S. Donati,²³
 R. B. Drucker,¹⁴ A. Dunn,¹⁶ K. Einsweiler,¹⁴ J. E. Elias,⁷ R. Ely,¹⁴ E. En-
 gels, Jr.,²² S. Eno,⁵ D. Errede,¹⁰ S. Errede,¹⁰ Q. Fan,²⁵ B. Farhat,¹⁵ I. Fiori,²
 B. Flaughner,⁷ G. W. Foster,⁷ M. Franklin,⁹ M. Frautschi,¹⁸ J. Freeman,⁷
 J. Friedman,¹⁵ H. Frisch,⁵ A. Fry,²⁹ T. A. Fuess,¹ Y. Fukui,¹³ S. Funaki,³¹
 G. Gagliardi,²³ S. Galeotti,²³ M. Gallinaro,²⁰ A. F. Garfinkel,²⁴ S. Geer,⁷
 D. W. Gerdes,¹⁶ P. Giannetti,²³ N. Giokaris,²⁶ P. Giromini,⁸ L. Gladney,²¹
 D. Glenzinski,¹² M. Gold,¹⁸ J. Gonzalez,²¹ A. Gordon,⁹ A. T. Goshaw,⁶
 K. Goulianos,²⁶ H. Grassmann,⁶ A. Grewal,²¹ G. Grieco,²³ L. Groer,²⁷
 C. Grosso-Pilcher,⁵ C. Haber,¹⁴ S. R. Hahn,⁷ R. Hamilton,⁹ R. Handler,³³
 R. M. Hans,³⁴ K. Hara,³¹ B. Harral,²¹ R. M. Harris,⁷ S. A. Hauger,⁶ J. Hauser,⁴
 C. Hawk,²⁷ J. Heinrich,²¹ D. Cronin-Hennessy,⁶ R. Hollebeek,²¹ L. Holloway,¹⁰
 A. Hölscher,¹¹ S. Hong,¹⁶ G. Houk,²¹ P. Hu,²² B. T. Huffman,²² R. Hughes,²⁵
 P. Hurst,⁹ J. Huston,¹⁷ J. Huth,⁹ J. Hylen,⁷ M. Incagli,²³ J. Incandela,⁷ H. Iso,³¹
 H. Jensen,⁷ C. P. Jessop,⁹ U. Joshi,⁷ R. W. Kadel,¹⁴ E. Kajfasz,^{7a} T. Kamon,³⁰
 T. Kaneko,³¹ D. A. Kardelis,¹⁰ H. Kasha,³⁴ Y. Kato,¹⁹ L. Keeble,³⁰
 R. D. Kennedy,²⁷ R. Kephart,⁷ P. Kesten,¹⁴ D. Kestenbaum,⁹ R. M. Keup,¹⁰
 H. Keutelian,⁷ F. Keyvan,⁴ D. H. Kim,⁷ H. S. Kim,¹¹ S. B. Kim,¹⁶

Submitted to Physical Review D March 6, 1995

S. H. Kim,³¹ Y. K. Kim,¹⁴ L. Kirsch,³ P. Koehn,²⁵ K. Kondo,³¹ J. Konigsberg,⁹
 S. Kopp,⁵ K. Kordas,¹¹ W. Koska,⁷ E. Kovacs,^{7a} W. Kowald,⁶ M. Krasberg,¹⁶
 J. Kroll,⁷ M. Kruse,²⁴ S. E. Kuhlmann,¹ E. Kuns,²⁷ A. T. Laasanen,²⁴
 N. Labanca,²³ S. Lammel,⁴ J. I. Lamoureux,³ T. LeCompte,¹⁰ S. Leone,²³
 J. D. Lewis,⁷ P. Limon,⁷ M. Lindgren,⁴ T. M. Liss,¹⁰ N. Lockyer,²¹ C. Loomis,²⁷
 O. Long,²¹ M. Loreti,²⁰ E. H. Low,²¹ J. Lu,³⁰ D. Lucchesi,²³ C. B. Luchini,¹⁰
 P. Lukens,⁷ P. Maas,³³ K. Maeshima,⁷ A. Maghakian,²⁶ P. Maksimovic,¹⁵
 M. Mangano,²³ J. Mansour,¹⁷ M. Mariotti,²³ J. P. Marriner,⁷ A. Martin,¹⁰
 J. A. J. Matthews,¹⁸ R. Mattingly,¹⁵ P. McIntyre,³⁰ P. Melese,²⁶ A. Menzione,²³
 E. Meschi,²³ G. Michail,⁹ S. Mikamo,¹³ M. Miller,⁵ R. Miller,¹⁷ T. Mimashi,³¹
 S. Miscetti,⁸ M. Mishina,¹³ H. Mitsushio,³¹ S. Miyashita,³¹ Y. Morita,¹³
 S. Moulding,²⁶ J. Mueller,²⁷ A. Mukherjee,⁷ T. Muller,⁴ P. Musgrave,¹¹
 L. F. Nakae,²⁹ I. Nakano,³¹ C. Nelson,⁷ D. Neuberger,⁴ C. Newman-
 Holmes,⁷ L. Nodulman,¹ S. Ogawa,³¹ S. H. Oh,⁶ K. E. Ohl,³⁴ R. Oishi,³¹
 T. Okusawa,¹⁹ C. Pagliarone,²³ R. Paoletti,²³ V. Papadimitriou,⁷ S. Park,⁷
 J. Patrick,⁷ G. Pauletta,²³ M. Paulini,¹⁴ L. Pescara,²⁰ M. D. Peters,¹⁴
 T. J. Phillips,⁶ G. Piacentino,² M. Pillai,²⁵ R. Plunkett,⁷ L. Pondrom,³³
 N. Produit,¹⁴ J. Proudfoot,¹ F. Ptohos,⁹ G. Punzi,²³ K. Ragan,¹¹ F. Rimondi,²
 L. Ristori,²³ M. Roach-Bellino,³² W. J. Robertson,⁶ T. Rodrigo,⁷ J. Romano,⁵
 L. Rosenson,¹⁵ W. K. Sakumoto,²⁵ D. Saltzberg,⁵ A. Sansoni,⁸ V. Scarpine,³⁰
 A. Schindler,¹⁴ P. Schlabach,⁹ E. E. Schmidt,⁷ M. P. Schmidt,³⁴ O. Schneider,¹⁴
 G. F. Sciacca,²³ A. Scribano,²³ S. Segler,⁷ S. Seidel,¹⁸ Y. Seiya,³¹ G. Sganos,¹¹
 A. Sgolacchia,² M. Shapiro,¹⁴ N. M. Shaw,²⁴ Q. Shen,²⁴ P. F. Shepard,²²
 M. Shimojima,³¹ M. Shochet,⁵ J. Siegrist,²⁹ A. Sill,^{7a} P. Sinervo,¹¹ P. Singh,²²
 J. Skarha,¹² K. Sliwa,³² D. A. Smith,²³ F. D. Snider,¹² L. Song,⁷ T. Song,¹⁶
 J. Spalding,⁷ L. Spiegel,⁷ P. Sphicas,¹⁵ A. Spies,¹² L. Stanco,²⁰ J. Steele,³³
 A. Stefanini,²³ K. Strahl,¹¹ J. Strait,⁷ D. Stuart,⁷ G. Sullivan,⁵ K. Sumorok,¹⁵
 R. L. Swartz, Jr.,¹⁰ T. Takahashi,¹⁹ K. Takikawa,³¹ F. Tartarelli,²³
 W. Taylor,¹¹ P. K. Teng,²⁸ Y. Teramoto,¹⁹ S. Tether,¹⁵ D. Theriot,⁷
 J. Thomas,²⁹ T. L. Thomas,¹⁸ R. Thun,¹⁶ M. Timko,³² P. Tipton,²⁵
 A. Titov,²⁶ S. Tkaczyk,⁷ K. Tollefson,²⁵ A. Tollestrup,⁷ J. Tonnison,²⁴
 J. F. de Troconiz,⁹ J. Tseng,¹² M. Turcotte,²⁹ N. Turini,² N. Uemura,³¹
 F. Ukegawa,²¹ G. Unal,²¹ S. van den Brink,²² S. Vejcek, III,¹⁶ R. Vidal,⁷
 M. Vondracek,¹⁰ R. G. Wagner,¹ R. L. Wagner,⁷ N. Wainer,⁷ R. C. Walker,²⁵
 C. H. Wang,²⁸ G. Wang,²³ J. Wang,⁵ M. J. Wang,²⁸ Q. F. Wang,²⁶
 A. Warburton,¹¹ G. Watts,²⁵ T. Watts,²⁷ R. Webb,³⁰ C. Wendt,³³ H. Wenzel,¹⁴
 W. C. Wester, III,¹⁴ T. Westhusing,¹⁰ A. B. Wicklund,¹ E. Wicklund,⁷
 R. Wilkinson,²¹ H. H. Williams,²¹ P. Wilson,⁵ B. L. Winer,²⁵ J. Wolinski,³⁰
 D. Y. Wu,¹⁶ X. Wu,²³ J. Wyss,²⁰ A. Yagil,⁷ W. Yao,¹⁴ K. Yasuoka,³¹ Y. Ye,¹¹
 G. P. Yeh,⁷ P. Yeh,²⁸ M. Yin,⁶ J. Yoh,⁷ T. Yoshida,¹⁹ D. Yovanovitch,⁷ I. Yu,³⁴

J. C. Yun,⁷ A. Zanetti,²³ F. Zetti,²³ L. Zhang,³³ S. Zhang,¹⁶ W. Zhang,²¹ and S. Zucchelli²

(CDF Collaboration)

- ¹ Argonne National Laboratory, Argonne, Illinois 60439
- ² Istituto Nazionale di Fisica Nucleare, University of Bologna, I-40126 Bologna, Italy
- ³ Brandeis University, Waltham, Massachusetts 02254
- ⁴ University of California at Los Angeles, Los Angeles, California 90024
- ⁵ University of Chicago, Chicago, Illinois 60637
- ⁶ Duke University, Durham, North Carolina 27708
- ⁷ Fermi National Accelerator Laboratory, Batavia, Illinois 60510
- ⁸ Laboratori Nazionali di Frascati, Istituto Nazionale di Fisica Nucleare, I-00044 Frascati, Italy
- ⁹ Harvard University, Cambridge, Massachusetts 02138
- ¹⁰ University of Illinois, Urbana, Illinois 61801
- ¹¹ Institute of Particle Physics, McGill University, Montreal H3A 2T8, and University of Toronto, Toronto M5S 1A7, Canada
- ¹² The Johns Hopkins University, Baltimore, Maryland 21218
- ¹³ National Laboratory for High Energy Physics (KEK), Tsukuba, Ibaraki 305, Japan
- ¹⁴ Lawrence Berkeley Laboratory, Berkeley, California 94720
- ¹⁵ Massachusetts Institute of Technology, Cambridge, Massachusetts 02139
- ¹⁶ University of Michigan, Ann Arbor, Michigan 48109
- ¹⁷ Michigan State University, East Lansing, Michigan 48824
- ¹⁸ University of New Mexico, Albuquerque, New Mexico 87131
- ¹⁹ Osaka City University, Osaka 588, Japan
- ²⁰ Università di Padova, Istituto Nazionale di Fisica Nucleare, Sezione di Padova, I-35131 Padova, Italy
- ²¹ University of Pennsylvania, Philadelphia, Pennsylvania 19104
- ²² University of Pittsburgh, Pittsburgh, Pennsylvania 15260
- ²³ Istituto Nazionale di Fisica Nucleare, University and Scuola Normale Superiore of Pisa, I-56100 Pisa, Italy
- ²⁴ Purdue University, West Lafayette, Indiana 47907
- ²⁵ University of Rochester, Rochester, New York 14627
- ²⁶ Rockefeller University, New York, New York 10021
- ²⁷ Rutgers University, Piscataway, New Jersey 08854
- ²⁸ Academia Sinica, Taiwan 11529, Republic of China
- ²⁹ Superconducting Super Collider Laboratory, Dallas, Texas 75237
- ³⁰ Texas A&M University, College Station, Texas 77843
- ³¹ University of Tsukuba, Tsukuba, Ibaraki 305, Japan
- ³² Tufts University, Medford, Massachusetts 02155
- ³³ University of Wisconsin, Madison, Wisconsin 53706

³⁴ *Yale University, New Haven, Connecticut 06511*

This paper presents a measurement of the mass of the W boson using data collected with the CDF detector during the 1992-93 collider run at the Fermilab Tevatron. A fit to the transverse mass spectrum of a sample of 3268 $W \rightarrow \mu\nu$ events recorded in an integrated luminosity of 19.7 pb^{-1} gives $M_W^\mu = 80.310 \pm 0.205 \text{ (stat.)} \pm 0.130 \text{ (syst.) GeV}/c^2$. A fit to the transverse mass spectrum of a sample of 5718 $W \rightarrow e\nu$ events recorded in 18.2 pb^{-1} gives $M_W^e = 80.490 \pm 0.145 \text{ (stat.)} \pm 0.175 \text{ (syst.) GeV}/c^2$. Combining the muon and electron results, accounting for correlated uncertainties, yields $M_W = 80.410 \pm 0.180 \text{ GeV}/c^2$.

Section 1

INTRODUCTION

The relations among the masses and couplings of gauge bosons allow incisive tests of the Standard Model of the electroweak interactions [1]. These relations are precisely specified at Born level; higher-order radiative corrections, which are sensitive to the top quark mass, M_{top} , and the Higgs boson mass, M_{Higgs} , have also been calculated [2]. Measurements of the properties of the Z boson, as well as measurements of atomic transitions, muon decay, and deep-inelastic scattering, tightly constrain the relationship between allowed values of M_{top} and the W mass, M_W [3]. Precise measurements of M_W and of M_{top} , if inconsistent with the allowed range of predictions, could indicate the existence of new phenomena at or above the electroweak scale. Alternatively, within the confines of the Standard Model, such measurements predict M_{Higgs} . The measurement of the W mass is unique among electroweak measurements in its sensitivity to charged currents at large momentum transfer.

The direct measurement of the W mass has to date been possible only at the antiproton-proton colliders at CERN and Fermilab, accelerators with sufficient center-of-mass energy to produce the W . A summary of previously published measurements is given in Table 1.1. We present here a new measurement with a precision twice that of the best previously published value.

Experiment	Reference	Mode	Mass (GeV/c ²)
UA1-83	[4]	$e\nu$	81 ± 5
UA2-83	[5]	$e\nu$	80^{+10}_{-6}
UA1-84	[6]	$\mu\nu$	81^{+6}_{-7}
UA1-86	[7]	$e\nu$	83.5 ± 2.9
UA2-87	[8]	$e\nu$	80.2 ± 1.5
UA1-89	[9]	$\mu\nu$	81.8 ± 6.5
UA1-89	[9]	$\tau\nu$	$89 \pm 3 \pm 6$
CDF-89	[10]	$e\nu$	80.0 ± 4.1
UA2-90	[11]	$e\nu$	80.53 ± 0.49
CDF-90	[12]	$e\nu, \mu\nu$	79.91 ± 0.39
UA2-92	[13]	$e\nu$	80.36 ± 0.37

Table 1.1: Some previously published W mass measurements. Not all of the above measurements are independent. The mode is the decay channel of the W used in the measurement.

This paper describes the measurement of the W mass using W bosons observed in antiproton-proton ($\bar{p}p$) collisions produced at the Fermilab Tevatron with a center-of-mass energy of 1800 GeV. The results are from an analysis of the decays of the W into a muon and neutrino in a data sample of integrated luminosity of 19.7 pb^{-1} , and decays of the W into an electron and neutrino in an 18.2 pb^{-1} subset, collected by the Collider Detector at Fermilab (CDF) during the period from August 1992 to May 1993.

The paper is structured as follows. A description of the detector and an overview of the analysis are given in Section 2. The calibration and alignment of the central tracking chamber, which provides the momentum scale for the mass measurement, is described in Section 3. Sections 4, 5, and 6 are largely parallel: Section 4 describes muon identification and the determination of the momentum resolution; Section 5 describes electron identification, the transfer of the momentum scale to the calorimeter energy scale, and the determination of the energy resolution; Section 6 describes the determination of the

detector response to hadrons recoiling against the W in the event, necessary to infer the neutrino momentum scale. The knowledge of the lepton and recoil responses is incorporated in a Monte Carlo model of W production and decay, described in Section 7. Section 8 describes the effects of background processes and radiative corrections on the mass measurement. Section 9 gives details of the fitting method used to extract the W mass from a comparison of the data and the model. Each of these sections ends with a summary of numerical results. Section 10 presents a global summary of the measured values and the experimental uncertainties. Finally, the measured W mass is compared to previous measurements and current predictions.

Section 2

OVERVIEW

This section begins with a discussion of how the nature of W boson production and decay motivates the strategy used to measure the W mass. The aspects of the detector critical to the measurement are then described. A brief description of the data samples used for the calibrations and for the mass measurement follows. A summary of the analysis strategy concludes the section.

2.1 Nature of W Events

The dominant mechanism for production of W bosons in antiproton-proton collisions is predicted to be antiquark-quark annihilation, with additional contributions from higher-order diagrams [14]. The W is produced with momentum in the transverse and longitudinal directions relative to the center-of-mass of the antiproton-proton collision¹. This momentum is balanced by the momentum of hadrons produced in association with the W , referred to as the “recoil”, as illustrated in Figure 2.1.

¹CDF uses a cylindrical coordinate system with the z (longitudinal) axis along the proton beam axis; r is the transverse coordinate, and ϕ is the azimuthal angle. Pseudorapidity (η) is defined as $\eta \equiv -\ln(\tan(\theta/2))$, where θ is the polar angle relative to the proton-beam direction. See Figure 2.2.

The W boson decays used in this analysis are the two-body leptonic decays producing an electron or muon and a neutrino. Since the apparatus cannot detect the neutrino and cannot measure the z -component of the recoil momentum, much of which is carried in fragments of the initial proton and anti-proton at small angles to the beams, there is insufficient information to reconstruct the invariant mass of the W on an event-by-event basis. Rather, this analysis uses the transverse mass of each W event, which is analogous to the invariant mass except that only the components of energy flow transverse to the beamline are used. Specifically,

$$(M_T^W)^2 = (E_T^\ell + E_T^\nu)^2 - (\mathbf{E}_T^\ell + \mathbf{E}_T^\nu)^2, \quad (2.1)$$

where M_T^W is the transverse mass of the W , E_T^ℓ is the transverse energy of the charged lepton (electron or muon), and E_T^ν is the transverse energy of the neutrino.² The boldface denotes two-component vector quantities. The transverse energy of the neutrino is not measured, but rather is inferred from momentum imbalance in the calorimeters,

$$\mathbf{E}_T^\nu = -(\mathbf{E}_T^\ell + \mathbf{u}), \quad (2.2)$$

where \mathbf{u} denotes the transverse energy vector of the recoil (see Figure 2.1).

When $|\mathbf{u}| \ll E_T^\ell$, the transverse mass measurement of Equation 2.1 becomes

$$M_T^W \approx 2E_T^\ell + u_{||}, \quad (2.3)$$

where $u_{||}$ is the transverse energy of the recoil projected along the direction of the charged lepton, $(\mathbf{u} \cdot \mathbf{E}_T^\ell)/E_T^\ell$. The resolutions on the measurements of the charged lepton energy and the recoil must be understood to make adequate predictions of the transverse mass shape; the distribution in u_{\perp} , the component perpendicular to $u_{||}$, is used as a sensitive test of the adequacy of the

²Although energy is a scalar quantity, “transverse energy” commonly denotes the transverse component of the vector whose *magnitude* is the energy of the particle and *direction* is parallel to the momentum of the particle.

modeling. In addition, effects which systematically bias $u_{||}$ must be accounted for. The transverse mass is invariant to first order under Lorentz boosts in the transverse direction; uncertainties associated with the W boson transverse momentum spectrum enter into the mass measurement primarily through mis-measurements of the W recoil transverse energy, u , and, to a lesser extent, through acceptance effects. Note that the approximation of Equation 2.3 is shown only to illustrate these points and that the true transverse mass is used everywhere in this analysis.

2.2 Detector

This section briefly describes those aspects of the CDF detector pertinent to the W mass measurement. A more detailed description can be found in Reference [15]; recent detector upgrades are described in References [16] and [17].

The CDF detector is an azimuthally and forward-backward symmetric magnetic detector designed to study $\bar{p}p$ collisions at the Tevatron. The magnetic spectrometer consists of tracking devices inside a 3-m diameter, 5-m long superconducting solenoidal magnet which operates at 1.4 T. The detector is divided into a central region ($30^\circ < \theta < 150^\circ$), end-plugs ($10^\circ < \theta < 30^\circ$, $150^\circ < \theta < 170^\circ$), which form the pole pieces for the solenoidal magnet, and forward/backward regions ($2^\circ < \theta < 10^\circ$, $170^\circ < \theta < 178^\circ$). Muon chambers are placed outside (at larger radius) of the hadronic calorimeters in the central region; toroidal steel magnets and chambers provide additional muon coverage and shielding on each end. An elevation view of one quarter of the CDF detector is shown in Figure 2.2.

2.2.1 Tracking Detectors

A four-layer silicon microstrip vertex detector (SVX) [17], used in this analysis to provide a precision measurement of the beam axis, is located directly outside the 1.9-cm radius beryllium beampipe. The four layers of the SVX are at radii of 3.0, 4.2, 5.7, and 7.9 cm from the beamline. Outside the SVX is a set of vertex time projection chambers (VTX) [18], which provides r - z tracking information out to a radius of 22 cm for $|\eta| < 3.25$. The VTX is used in this analysis for finding the z position of the antiproton-proton interaction (the event vertex). The event vertex is necessary for event selection, lepton track reconstruction, and the calculation of E_T . Both the SVX and VTX are mounted inside the central tracking chamber (CTC) [19], a 3.2-m long drift chamber that extends in radius from 31.0 cm to 132.5 cm. The CTC has 84 sampling wire layers, organized in 5 axial and 4 stereo “super-layers” [19]. Axial super-layers have 12 radially separated layers of sense wires, parallel to the z axis, that measure the r - ϕ position of a track. Stereo super-layers have 6 sense wire layers, with a $\sim 3^\circ$ stereo angle, that measure a combination of r - ϕ and z information. The stereo angle direction alternates at each stereo super-layer. Axial and stereo data are combined to form a 3-dimensional track. In this analysis, the electron or muon momentum is measured from the curvature, azimuthal angle, and polar angle of the track as the particle traverses the magnetic field. The CTC momentum measurement is the ultimate source of all energy calibrations in this experiment. Details of the calibration and alignment of the CTC are given in Section 3.

2.2.2 Calorimeters

The electromagnetic and hadronic calorimeters subtend 2π in azimuth and from -4.2 to 4.2 in pseudorapidity (η). The calorimeters are constructed with a projective tower geometry, with towers subtending ap-

proximately 0.1 in pseudorapidity by 15° in ϕ (central) or 5° in ϕ (plug and forward). Each tower consists of an electromagnetic calorimeter followed by a hadronic calorimeter at larger radius. The energies of central electrons, used in the mass measurement, are measured from the electromagnetic shower produced in the central electromagnetic calorimeter (CEM) [20]. The central calorimeter is constructed as 24 “wedges” in ϕ for each half of the detector ($-1.1 < \eta < 0$ and $0 < \eta < 1.1$). Each wedge has 10 electromagnetic towers, which use lead as the absorber and scintillator as the active medium, for a total of 480 CEM towers.³ A proportional chamber measures the electron shower position in the ϕ and z directions at a depth of ~ 6 radiation lengths in the CEM [20]. For the purposes of triggering and data sample selection, the CEM calibrations are derived from testbeam data taken during 1984-85. To compensate for scintillator aging, the tower gains were corrected in March 1992 using Cesium-137 gamma-ray sources. Details of the calibration of the CEM are given in Section 5.

The central calorimeters also measure the energy flow of particles produced in association with the W . Outside the CEM is a similarly segmented hadronic calorimeter (CHA) [21]. Electromagnetic and hadronic calorimeters which use multi-wire proportional chambers as the active sampling medium extend this coverage to $|\eta| = 4.2$ [22]. In this analysis, however, the recoil energy is calculated only in the region of full azimuthal symmetry, $|\eta| < 3.6$. Understanding the response of these devices to the recoil from bosons is problematic as it depends on details of the flow and energy distributions of the recoil hadrons. Instead, the energy response to recoil energy is mapped out using $Z \rightarrow ee$ events. Details of the calibration of the calorimeters to recoil energy are given in Sections 6 and 7.

³There are actually only 478 physical CEM towers; the locations of two towers are used for the cryogenic penetrations for the magnet.

2.2.3 Muon Detectors

Four layers of drift chambers, embedded in the wedge directly outside (in radius) of the CHA, form the central muon detection system (CMU) [23]. The CMU covers the region $|\eta| < 0.6$. Outside of these systems there is an additional absorber of 0.6 m of steel followed by a system of four layers of drift chambers (CMP). Approximately 84% of the solid angle for $|\eta| < 0.6$ is covered by CMU, 63% by CMP, and 53% by both. Muons from W decay are required in this analysis to produce a track in the CMU that matches a track in the CTC. The CMP is used in this measurement only in the Level 1 and Level 2 triggers. Details of the muon selection and reconstruction are given in Section 4.

2.2.4 Trigger and Data Acquisition

The CDF trigger is a three-level system that selects events for recording to magnetic tape. The crossing rate of proton and antiproton bunches in the Tevatron is 286 kHz, with a mean interaction rate of 0.6 interactions per crossing at a luminosity of $3.6 \times 10^{30} \text{ cm}^{-2} \text{ sec}^{-1}$, typical of the data presented here. The first two levels of the trigger [24] consist of dedicated electronics with separate data paths from the data acquisition system. The third level [25], which is initiated after the event information is digitized and stored, uses a farm of commercial computers to reconstruct events. The overall rejection factors for each of the three levels are typically 600, 100, and 4, respectively. At Level 1, electrons are selected by the presence of a single calorimeter tower above a threshold; muons are selected by the presence of a track in the CMU, and where there is full coverage, also in the CMP. At Level 2, electrons from W decay can satisfy one of a number of triggers. Some require a track to be found in the r - ϕ plane by a fast hardware processor [26] and to match to a calorimeter cluster; others have no track requirement but

require a high- E_T cluster[24]. The muon Level 2 trigger requires a track with large transverse momentum (p_T) that matches to a muon chamber track. At Level 3, reconstruction programs that include three-dimensional track reconstruction identify high- p_T electrons or muons.

Events that pass the Level 3 triggers are sorted and recorded. A subset of events, typically those from rarer processes (such as W decay), is written to disk in a separate data stream as well as being recorded to magnetic tape with the bulk of the events. These events are reconstructed rapidly after the data are taken, and, being a smaller sample, are more easily available for analysis. All of the data samples below, with the exception of the inclusive electrons and the Υ samples, come from this data stream.

The data used in this analysis come from a recorded integrated luminosity of 19.7 pb^{-1} [27]. A requirement that the data not have been recorded immediately after a long collision hall access, when the CEM phototube gains were unstable, removes 1.5 pb^{-1} from the electron sample.

2.3 Data Samples

Seven data samples are employed in this analysis. These are described briefly below and in more detail in subsequent sections as they are used. A list of the samples follows:

- **The $J/\psi \rightarrow \mu\mu$ sample.** A sample of $\sim 60,000$ $J/\psi \rightarrow \mu\mu$ candidates is used to determine the absolute momentum scale from a measurement of the J/ψ mass, and to set limits on systematic effects associated with track reconstruction.
- **The $\Upsilon \rightarrow \mu\mu$ sample.** A sample of ~ 2000 $\Upsilon \rightarrow \mu\mu$ candidates serves as a check on the momentum scale.

- **The $Z \rightarrow \mu\mu$ sample.** A sample of 330 dimuon events near the Z mass measures the momentum resolution from the width of the Z peak. The sample also serves as an additional check of the momentum scale.
- **The $W \rightarrow \mu\nu$ sample.** A sample of 3268 $W \rightarrow \mu\nu$ candidates is used to measure the W mass.
- **The inclusive electron sample.** A sample of $\sim 140,000$ central electrons with $E_T > 9$ GeV is used to understand the response of the central electromagnetic calorimeter (CEM) up to an overall normalization. A high- E_T subset of these events is used to align the CTC.
- **The $W \rightarrow e\nu$ sample.** A sample of 5718 $W \rightarrow e\nu$ candidates is used to set the absolute CEM energy scale from the momentum scale, and to measure the W mass.
- **The $Z \rightarrow ee$ sample.** A sample of 555 dielectron events near the Z mass is used to map out the response of the calorimeters to W boson recoil. A subset of this sample, 259 events where both electrons land in the CEM, measures the energy resolution and serves as a check of the energy scale.

2.4 Strategy of the Analysis

The determination of the momentum and energy scales⁴ is crucial to the W mass measurement. Momentum is the kinematic quantity necessarily measured for muons; for electrons, the energy as measured in the calorimeter is the quantity of choice as it is much less sensitive than the momentum to the effects of bremsstrahlung [28]. The basic architecture of the CDF detector is a calorimeter behind a magnetic spectrometer. The spectrometer measures

⁴Throughout this paper, momentum measurements using the CTC are denoted as p , and calorimeter energy measurements are denoted as E .

the momentum of muons and electrons, and the calorimeter measures the energy of electrons. This configuration allows *in situ* calibrations of both the momentum and energy scales directly from the collider data. The alignment of the CTC wires is done with high momentum electrons, exploiting the charge independence of the electromagnetic calorimeter measurement (both positives and negatives should give the same momentum for a given energy). The momentum scale of the magnetic spectrometer is then calibrated using the reconstructed mass of the $J/\psi \rightarrow \mu\mu$ resonance. Conversely, the calorimeter is calibrated by normalizing the average calorimeter response to electrons (both e^+ and e^-) of a given momentum, exploiting the uniformity, stability, and linearity of the magnetic spectrometer. The momenta of lepton tracks from W decays reconstructed with the final CTC calibration typically change from the initial values used for data sample selection by less than 10%; the mean changes by less than 0.1%. The final CEM calibration differs tower-by-tower from the initial calibration on average by less than 1%, with an RMS spread of 3.5%.

The detector response to the recoil $|\mathbf{u}|$ is directly calibrated using $Z \rightarrow ee$ decays, in which the electron energies are well measured. This sample is used as a table from which one can look up the measured response $|\mathbf{u}|$ for a given p_T^Z . We assume that the response to the recoil from a Z of a given p_T is the same as that to the recoil from a W of the same p_T .

The observed transverse mass lineshape also depends on the transverse and longitudinal W momentum spectra, and the resolutions in momentum (for muons) and energy (for electrons). As an initial guess for the p_T^W spectrum, the observed $Z \rightarrow ee$ p_T spectrum, corrected for the effect of electron energy resolution, is used. This spectrum is tuned for consistency with the observed u_\perp distribution. The longitudinal W momentum spectrum is constrained by restricting the choice of parton distribution functions to those consistent with the CDF W charge asymmetry measurement [29]. The mo-

momentum resolution is determined from the width of the $Z \rightarrow \mu\mu$ mass peak. The energy resolution is determined from the width of the $Z \rightarrow ee$ peak.

To extract the W mass, the measured W transverse mass spectrum is fit to transverse mass spectra simulated by Monte Carlo for a range of W masses and widths. Backgrounds are included in the simulated lineshapes. The mass shift due to electromagnetic radiative processes is calculated by Monte Carlo and is applied to the fitted mass. The uncertainties associated with known systematic effects are estimated by varying the magnitude of these effects within the Monte Carlo simulation and refitting the data.

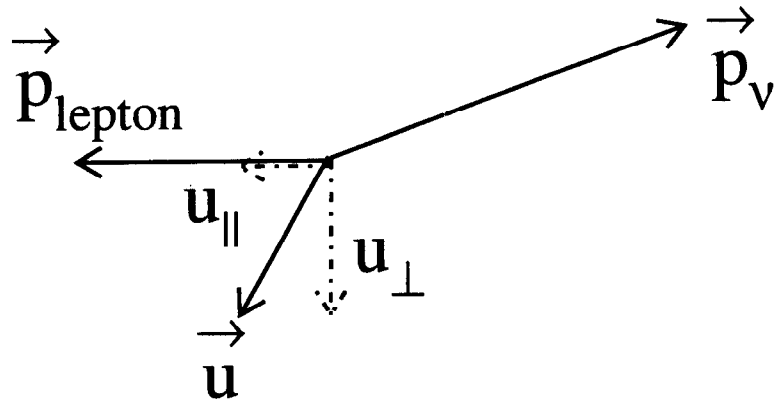


Figure 2.1: Kinematics of W boson production and decay for the events used in this analysis, as viewed in the plane transverse to the antiproton-proton beams. The vector \mathbf{u} denotes the transverse energy vector of the recoil.

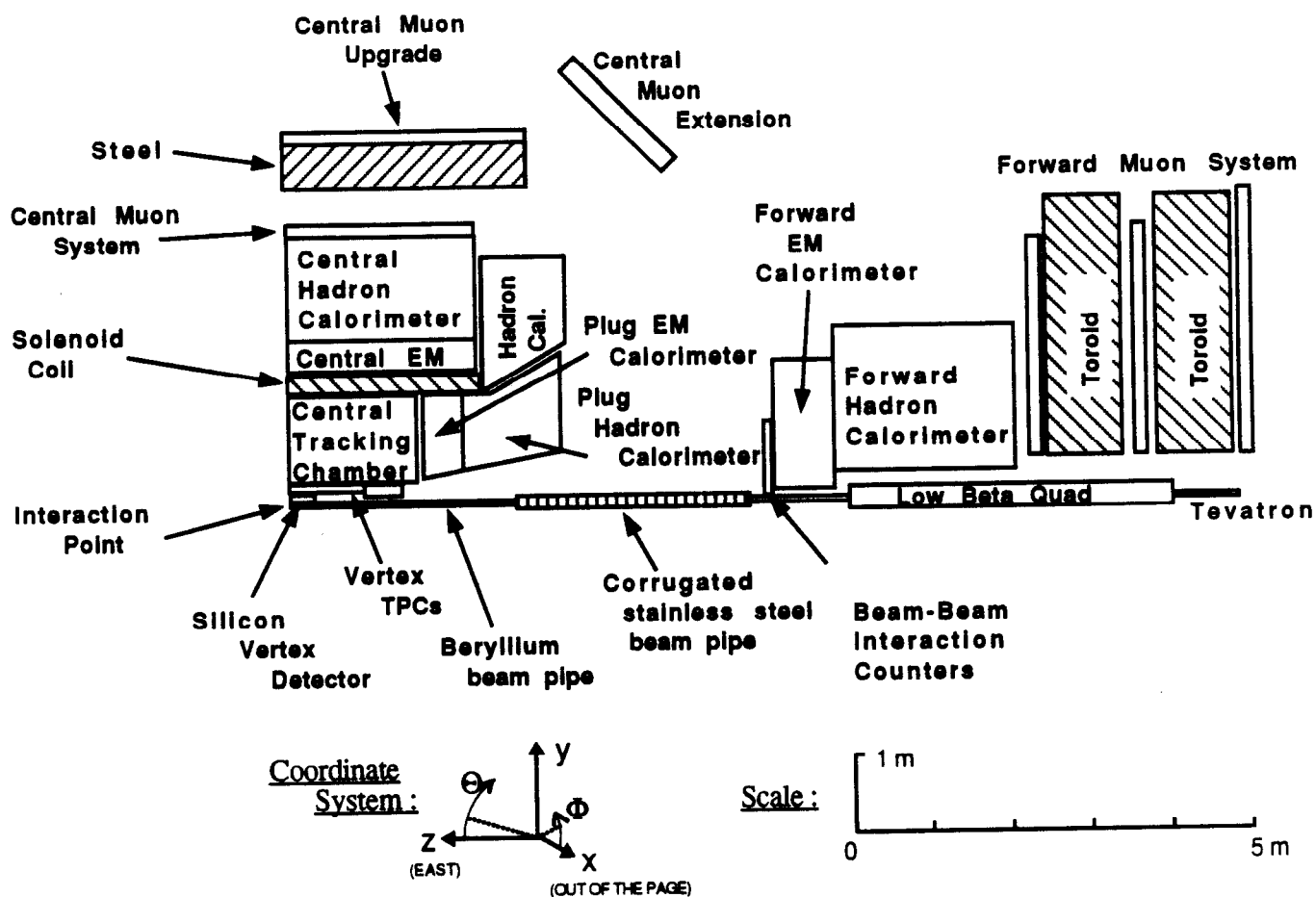


Figure 2.2: One quarter of the CDF detector. The detector is symmetric about the interaction point.

Section 3

MOMENTUM SCALE

In this section, the reconstruction of charged-particle trajectories and momenta using the central tracking chamber (CTC) is presented. The CTC calibration and alignment, and the determination of the absolute momentum scale using the $J/\psi \rightarrow \mu\mu$ resonance are described. Checks of the momentum scale from direct measurements of the $\Upsilon \rightarrow \mu\mu$ and $Z \rightarrow \mu\mu$ masses are given.

3.1 Track Reconstruction

The momentum of a charged particle is determined from its trajectory in the CTC. The CTC is operated in an axial magnetic field, uniform to within $\sim 1\%$. In a uniform field charged particles follow a helical trajectory. This helix is parametrized by: curvature, C (inverse diameter of the circle in r - ϕ); impact parameter, D_0 (distance of closest approach to $r = 0$); ϕ_0 (azimuthal direction at the point of closest approach to $r = 0$); z_0 (the z position at the point of closest approach to $r = 0$); and $\cot \theta$, where θ is the polar angle. The helix parameters are determined taking into account the non-uniformities of the magnetic field using the magnetic field map (see Section 3.3). The absolute

scale of the magnetic field was measured by inserting an NMR probe into a precise point in the tracking volume at the end of the data-taking period [30].

The momentum resolution is improved by a factor of two by constraining tracks to originate from the interaction point in the r - ϕ plane (the “beam constraint”). The z location of the interaction point (the ‘event vertex’) is determined by the VTX for each event with a precision of 1 mm. The distribution of event vertices has an RMS spread of 25–30 cm, depending on accelerator conditions. The r - ϕ location of the beam axis is measured by the SVX as a function of z with a precision of 10 μm . The beam axis is tilted with respect to the CTC axis by a slope that is about 400 microns per meter.

The measured muon momenta from $J/\psi \rightarrow \mu\mu$ decay are corrected for ionization energy loss (dE/dx) in traversing the $(8.9 \pm 0.9)\%$ of a radiation length of material (X_0) between the event vertex and the CTC tracking volume (See Section 5.6). The correction for this energy loss is negligible for the $W \rightarrow \mu\nu$ mass measurement, but is significant for the precision reconstruction of the J/ψ mass, used to normalize the momentum scale. For electrons, the effect of bremsstrahlung is not included in the electron track reconstruction, but is dealt with in the procedure used to transfer the momentum scale to the calorimeter energy scale, discussed in Section 5.

3.2 Calibration and Alignment

The CTC calibration and alignment proceeds in three steps. First, the relationship between the measured drift time and the distance to the sense wire is established. Second, the relative alignment of wires and layers in the CTC is performed. The final step is a fine-tuning of the alignment.

3.2.1 Time-to-distance calibration

Electronic pulsing, performed periodically during the data-taking period, gives relative time pedestals for each sense wire. Variations in drift properties for each super-layer are removed run-by-run [31]. Additional corrections for non-uniformity in the drift trajectories are made based on data from many runs. For each primary vertex found by the VTX, an interaction time is measured from the associated tracks. This procedure accounts for the variation of the interaction time, as well as for any drift in cable delays. After calibration, the CTC drift-distance resolution is determined to be $170\ \mu\text{m}$ (outer layers) to $220\ \mu\text{m}$ (inner layers), to be compared with $\sim 120\ \mu\text{m}$ expected from diffusion alone, and $\sim 200\ \mu\text{m}$ expected from test-chamber results.

3.2.2 Wire and layer alignment

The initial individual wire positions are taken to be the nominal positions determined during the CTC construction [19]. The distribution of differences between these nominal positions and the positions determined with an optical survey has an RMS of $25\ \mu\text{m}$. The 84 layers of sense wires are aligned relative to each other by requiring the ratio of energy to momentum E/p for electrons to be independent of charge.¹ A sample of about 10,000 inclusive electrons with $E_T > 18\ \text{GeV}$ is used for this alignment procedure. The alignment consists of rotating each entire layer on each end of the CTC by a different amount $r \times \Delta\phi$. The measured deviation of each layer from its nominal position after this alignment is shown in Figure 3.1.

3.2.3 Fine-tuning

The $W \rightarrow e\nu$ mass sample (see Section 5.3) is used to fine-tune the CTC alignment. The fine-tuning removes residual global ϕ -dependent and θ -

¹For convenience, the requisite factor of c is dropped in the ratio E/p .

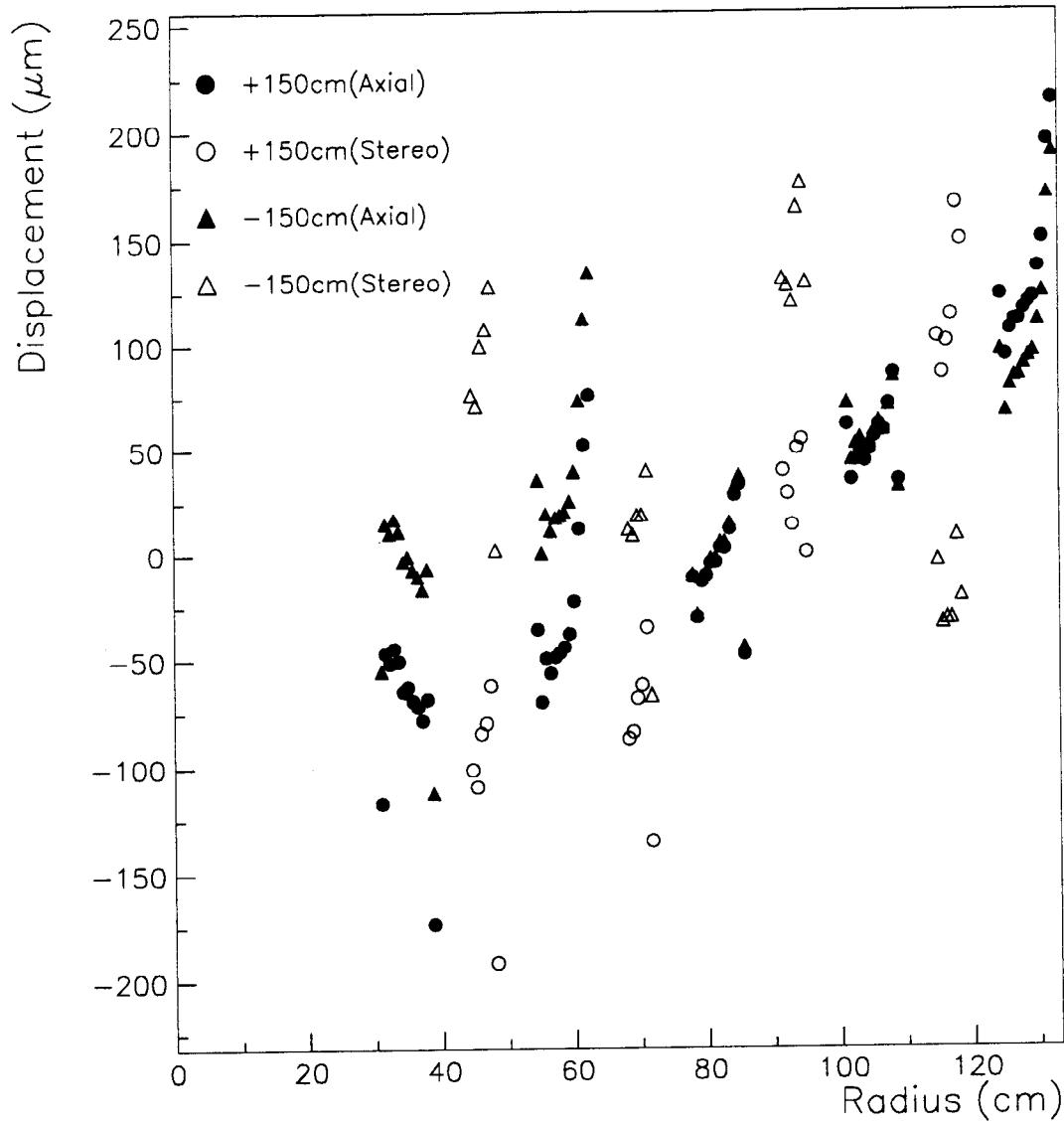


Figure 3.1: The deviation ($r \times \Delta\phi$) of each CTC layer from its nominal position at the end plates ($|z| = 150$ cm), versus the radius of the layer, r .

dependent charge splittings of $\langle E/p \rangle$, using many fewer parameters than the CTC layer alignment. The overall difference in $\langle E/p \rangle$ for the e^+ and e^- in this sample is $(0.06 \pm 0.12)\%$, which is consistent with zero. Note that a 0.12% difference in $\langle E/p \rangle$ corresponds to a curvature distortion equivalent to displacing the outermost wire layer by about $8 \mu\text{m}$ in azimuth. A ϕ -modulated charge difference in $\langle E/p \rangle$, which results from a residual misalignment of the CTC with respect to the beam axis, is observed. This modulation is removed with a correction of the form

$$\delta(1/p_T) = -0.00025 \times \sin(\phi - \phi_0), \quad (3.1)$$

where ϕ_0 is 3.6 radians and the coefficient corresponds to a beam position displacement of $30 \pm 10 \mu\text{m}$. A residual charge difference in $\langle E/p \rangle$ that varies with z and θ is also observed. Assuming this is due to a rotation at each endplate of the outer radius of the CTC with respect to the inner radius, a correction of the form

$$\delta(1/p_T) = -0.00035 \times (\cot \theta + z_{\text{vertex}}/187), \quad (3.2)$$

with z_{vertex} in centimeters, is used. This corresponds to a curvature distortion equivalent to a wire displacement (at $\cot \theta = 1.0$, using $z_{\text{vertex}} = 0$) of $80 \pm 25 \mu\text{m}$. Other reasonable models of CTC twist could have been used without a significant difference in the correction.

Residual misalignments of the CTC wires can cause a systematic error on the W mass. Specifically, a residual modulation in θ , such as the one described in Equation 3.2, would introduce a momentum scale bias arising from the forward-backward charge asymmetry in W decay [32]. The systematic uncertainty due to the residual θ -dependence is studied using the simulation described in Section 7. Residual misalignments consistent with the statistical precision on the parameters in Equation 3.2 could contribute up to a 0.02% scale uncertainty, corresponding to $15 \text{ MeV}/c^2$ on the W mass. This is taken

Effect	Uncertainty (MeV/c ²)
Statistics	0.1
Muon energy loss before tracking	1.3
Beam constraint	0.3
Opening polar angle effect	—
Residual field non-uniformity	0.6
Background	0.1
Time variation	0.5
Radiative decay	0.2
Uncertainty in world-average $M_{J/\psi}$	0.1
SUBTOTAL	1.6
Extrapolation from $M_{J/\psi}$ to M_W	0.9
TOTAL	1.8

Table 3.1: Uncertainties on using the J/ψ mass to set the momentum scale for electrons and muons from W decays, expressed as the uncertainty on the J/ψ mass in MeV/c². The tabulation includes the uncertainty incurred when extrapolating from tracks in J/ψ decays to tracks with zero curvature.

as an uncertainty common to the electron and muon analyses. Figure 3.2 shows the E/p distributions for e^+ and e^- after all alignments.

3.3 Momentum Scale Determination

The momentum scale is determined by normalizing the observed $J/\psi \rightarrow \mu\mu$ peak to the world-average mass [34]. The invariant mass spectrum of 60,000 muon pairs from J/ψ decay is shown in Figure 3.3. A list of the systematic uncertainties on using the J/ψ mass to set the momentum scale is given in Table 3.1. The tabulation includes the uncertainty incurred when extrapolating from the momenta characteristic of J/ψ decay to the momenta of leptons from W decays, expressed as an uncertainty on the J/ψ mass. The entries in the table are described below in the order they appear.

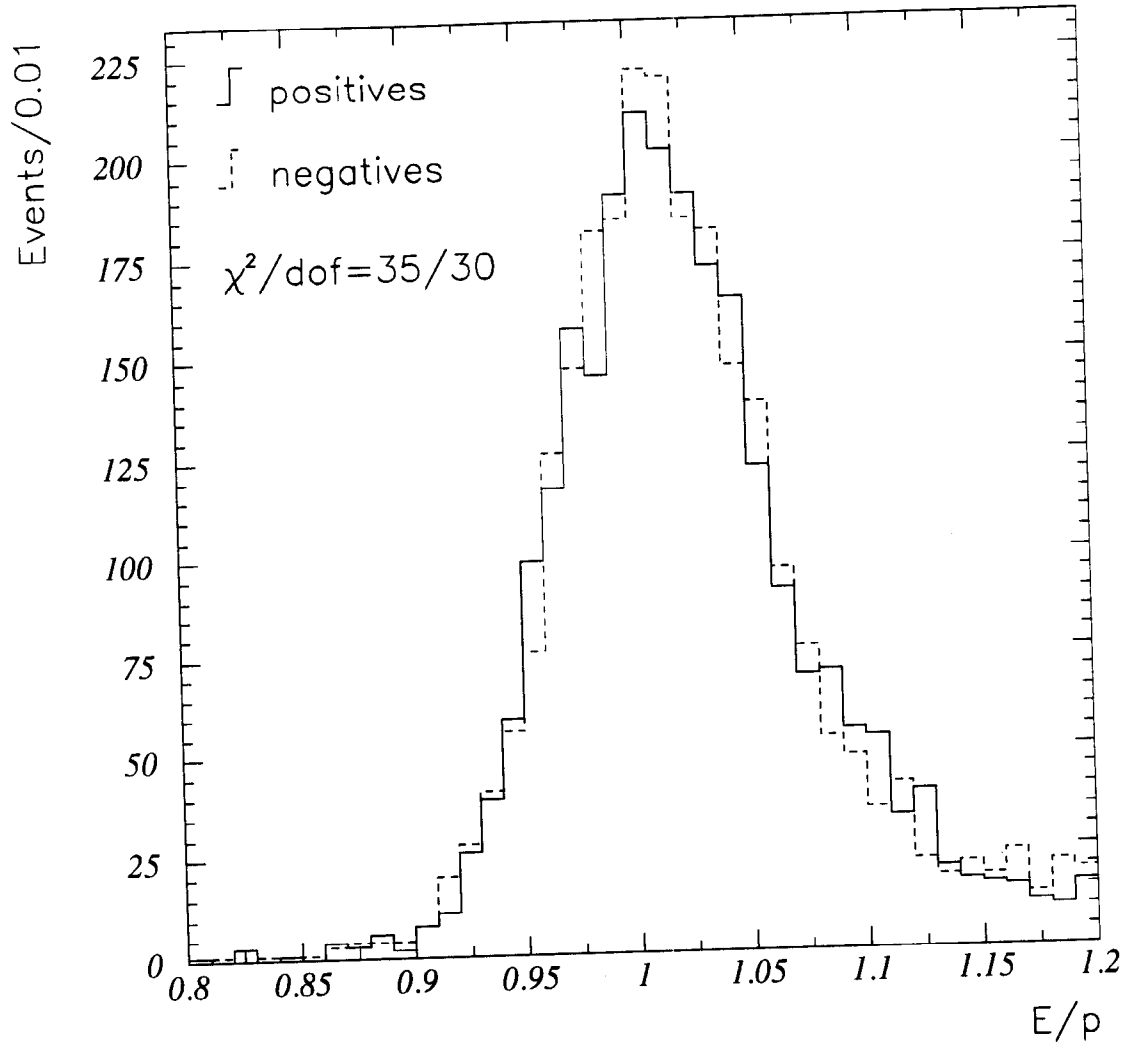


Figure 3.2: The ratio of E/p for central e^+ (solid) and e^- (dashed) in the $W \rightarrow e\nu$ sample after all CTC alignments and the beam constraint. The energy, E , used is calculated after all CEM calibrations have been performed [33].

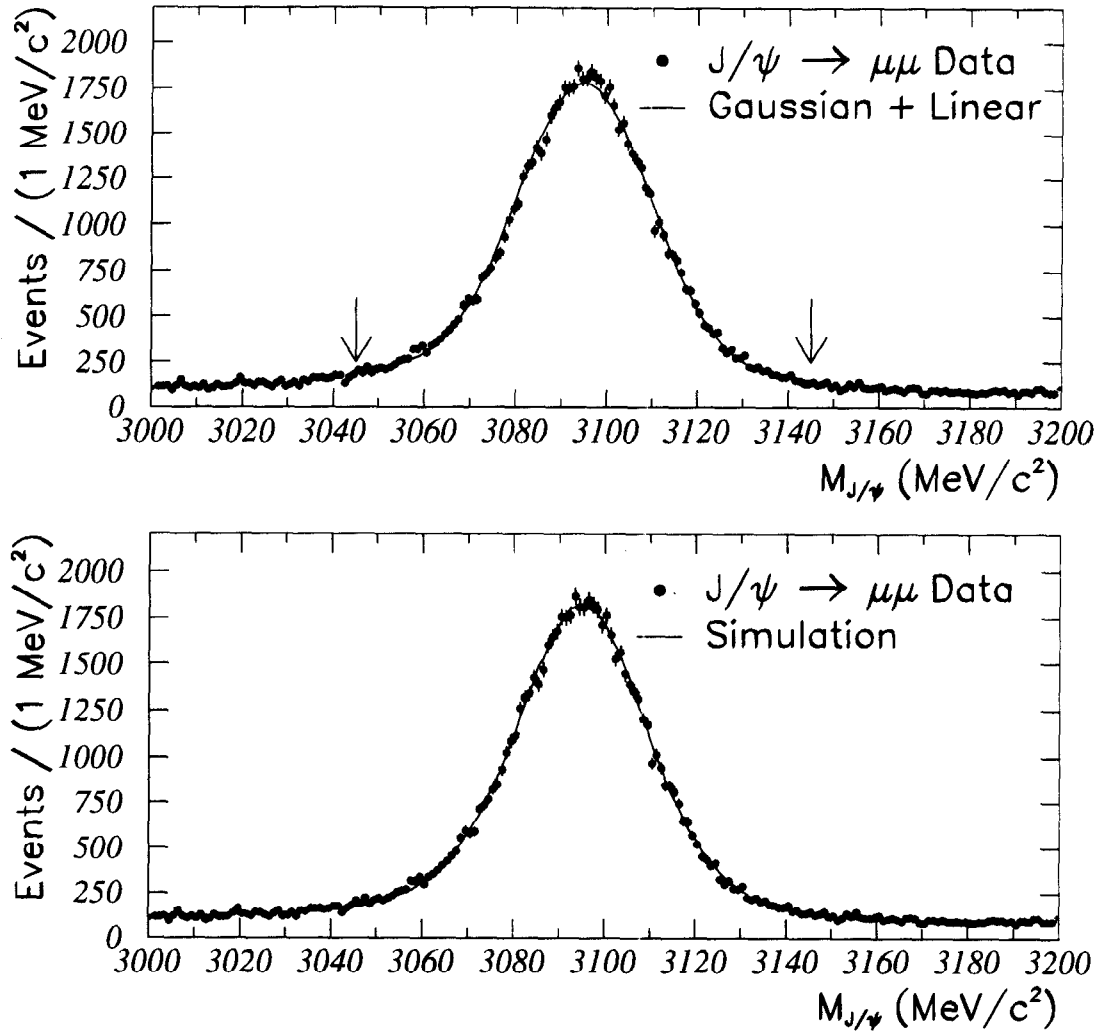


Figure 3.3: The measured dimuon mass spectrum (points), near the J/ψ mass in a 200 MeV/c² window. Upper: The curve is a Gaussian fit with a linear background in a 100 MeV/c² window. The arrows delimit the fit region. Lower: The curve is a Monte Carlo simulation including radiative effects.

Statistics: The J/ψ data are fit to a Gaussian with a linear background in a $100 \text{ MeV}/c^2$ window centered on the world-average mass. The fit determines the mean with a statistical accuracy of $0.1 \text{ MeV}/c^2$. Fits using wider windows yield shifts in the mass consistent with expected shifts due to the radiative tail. A fit to the shape derived from a simulation that includes radiative effects gives a consistent result (see Figure 3.3).

Muon Energy Loss: The momentum of each muon is corrected for energy loss in the material traversed by the muon. The amount of material is measured in radiation lengths from the tail of the E/p distribution for W electrons (see Section 5). For a given radiation length, the muon energy loss has a dependence on the type of material. A correction is made to the J/ψ mass based on the measured material. An uncertainty is calculated from the uncertainty in the amount and the type of material. The J/ψ mass correction due to energy loss is $3.7 \pm 1.2 \text{ MeV}/c^2$.

Beam Constraint: Since many J/ψ mesons come from decays of B mesons, which decay some distance from the primary vertex, the measured J/ψ peak may be shifted by the application of the beam constraint. The difference in the J/ψ mass between a fit using the beam constraint and a fit using only a constraint that the two muons originate from the same point is $0.3 \text{ MeV}/c^2$. This difference is taken as an uncertainty.

Opening Polar Angle: A dependence of the measured J/ψ mass on the opening polar angle ($\Delta \cot \theta = \cot \theta_{\mu^+} - \cot \theta_{\mu^-}$) between the two muons is observed (see Figure 3.4). For the purpose of studying the systematics on the J/ψ mass only, the stereo angle dependence is reduced by scaling $\cot \theta$ as follows:

$$\cot \theta \text{ (scaled)} = 0.999 \times \cot \theta. \quad (3.3)$$

The W mass measurement (as opposed to the J/ψ mass measurement) does

not use this $\cot \theta$ scaling since only the scale for transverse momentum is critical [35]. To keep the momentum scale determination independent of polar-angle effects, the mass is fitted versus $\Delta \cot \theta$ to a quadratic and the value at $\Delta \cot \theta = 0$ is used to determine the J/ψ mass [36].

Residual Field Non-Uniformity: The variations of the magnetic field both in magnitude and direction are small within the CTC active volume; $|\mathbf{B}(\mathbf{r}) - B(0) \hat{\mathbf{z}}|/B(0)$ has a maximum value of a few percent, occurring at the outer radius of the endplates of the CTC. Corrections to the track parameters for the field non-uniformity are based on a mapping of the field done in 1986, using a rotating search coil at a solenoid current of 5000 A [37]. During the data-taking period, the solenoid was actually run at a current of 4650 A. Due to saturation in the iron return yoke, the magnetic field is not exactly proportional to the solenoid current. A model of the iron structure and its saturation properties is used to correct for this, with the largest deviation from a simple scaling by 4650/5000 being 0.2% near the outer edge in z of the CTC. The model has been checked using search coil data taken at a few points with the solenoid at 4500 A, with agreement to within the measurement uncertainty of 2×10^{-4} T. The effect of the combined mapping and saturation corrections on the J/ψ mass is shown in Figure 3.5, as a function of $\cot \theta_{\mu^+} + \cot \theta_{\mu^-}$. The effects of any residual field non-uniformity are sought by looking at the variation of the J/ψ mass as a function of $\Sigma z^2 = z_{\mu^+}^2 + z_{\mu^-}^2$, where z is the track position at a radius of 100 cm. The mass is plotted as a function of Σz^2 in Figure 3.5 and the deviations are fit to a line [38]. The difference across the fit region is $0.6 \text{ MeV}/c^2$, which is taken as the uncertainty on the J/ψ mass.

Background: The uncertainty of the measured J/ψ mass due to uncertainty in the background shape is estimated by fitting both linear and quadratic background shapes to the data. It is determined to be less than $0.1 \text{ MeV}/c^2$.

Time Variation: An unexplained time variation of the J/ψ mass is observed

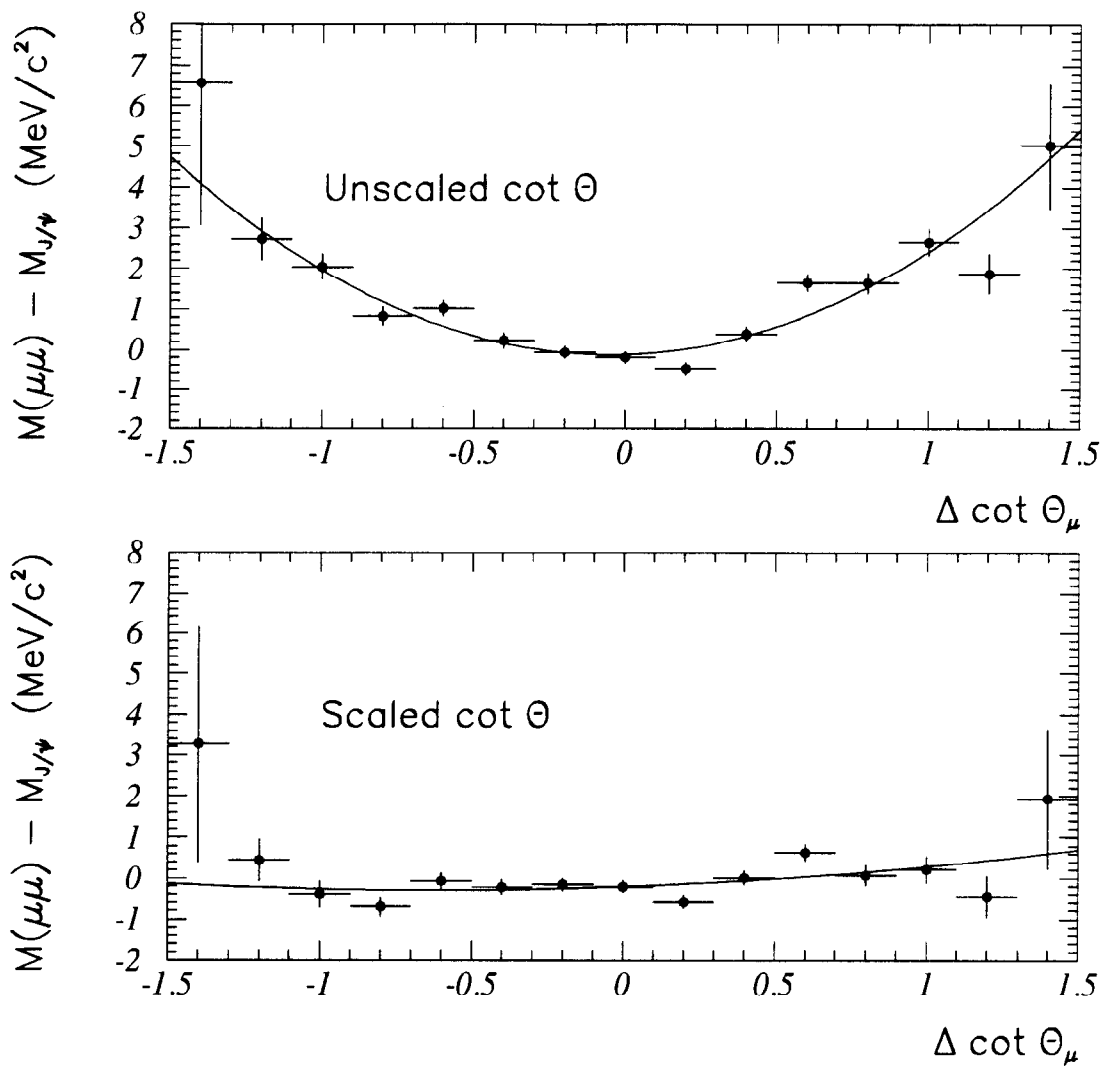


Figure 3.4: The variation of the measured J/ψ mass with $\Delta \cot \theta$ before (Upper) and after (Lower) scaling $\cot \theta$. The lines represent a quadratic fit.

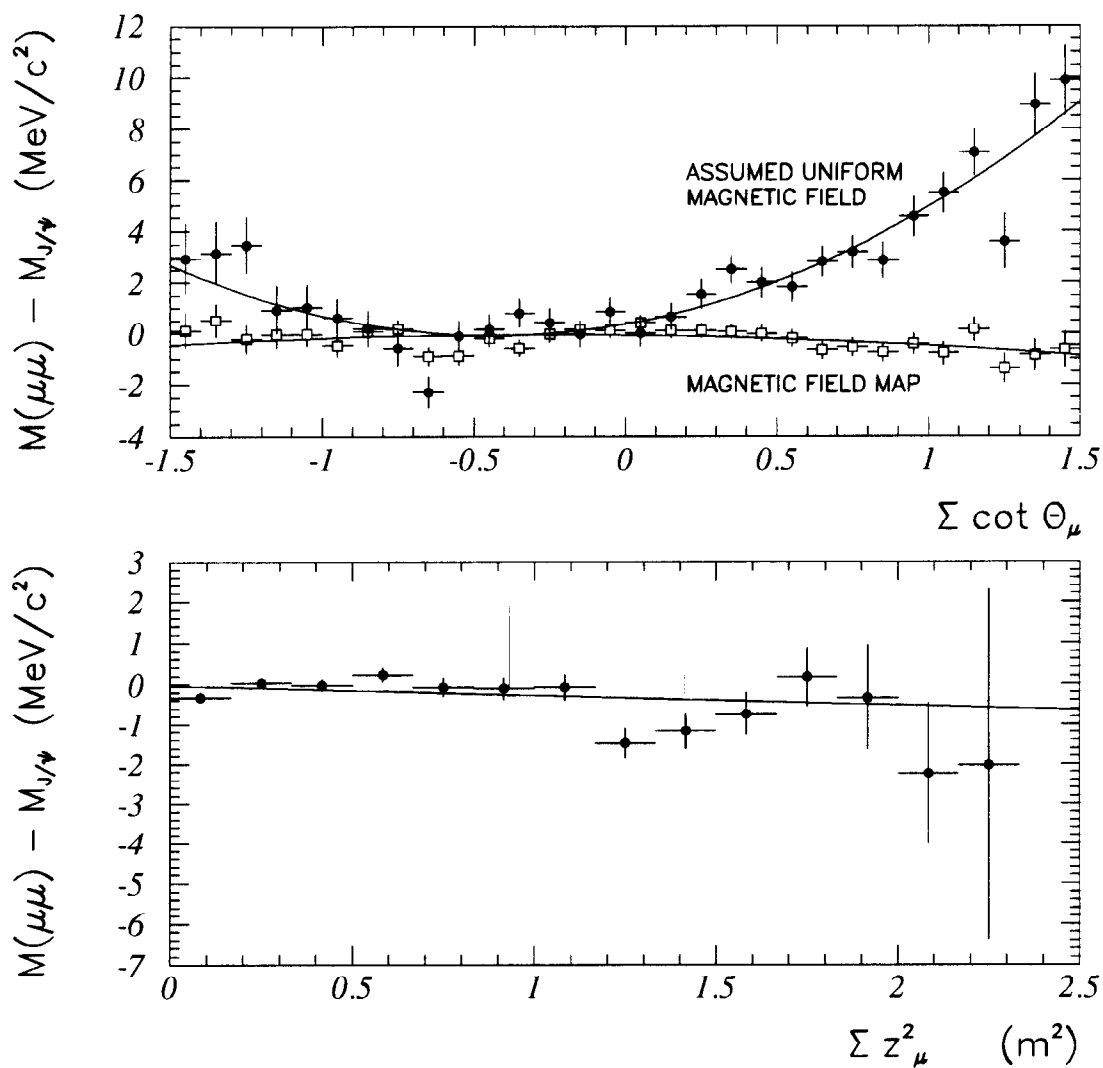


Figure 3.5: Upper: The variation of the measured J/ψ mass with $\cot \theta_{\mu^+} + \cot \theta_{\mu^-}$ before (solid) and after (open) applying the magnetic field map correction. Lower: The variation of the measured J/ψ mass with $\Sigma z^2 = z_{\mu^+}^2 + z_{\mu^-}^2$ where z is measured at a radius of 100 cm.

over the data-taking period as shown in Figure 3.6. The RMS deviation, $0.5 \text{ MeV}/c^2$, is taken as a systematic uncertainty. If this variation is due solely to changes in the magnetic field, then the effect is properly averaged by the procedure of setting the momentum scale, and no uncertainty would need to be taken.

Radiative Decay: The measured mass must be corrected for QED radiative effects in J/ψ decay. The correction is determined using Monte Carlo simulation (see Figure 3.3) to be $0.56 \pm 0.20 \text{ MeV}/c^2$. The systematic uncertainty represents possible variations from kinematics, modeling of resolutions, fitting procedures, and the background shape.

Uncertainty in the World-Average $M_{J/\psi}$: The uncertainty in the world-averaged J/ψ mass, $0.04 \text{ MeV}/c^2$, is included [34].

Extrapolation from $M_{J/\psi}$ to M_W : The momentum scale is set using muons from J/ψ decays in which the average muon p_T is $\sim 3 \text{ GeV}/c$. The average muon p_T from W decay is $\sim 38 \text{ GeV}/c$. However, the CTC does not directly measure momentum, but curvature, *i.e.*, inverse momentum, for which the difference between the J/ψ and the W is much smaller than the range in the J/ψ data. The most likely forms for non-linearity in the CTC momentum measurement are linear in the average $1/p_T^2$ of the two muons [39]. Figure 3.7 shows the variation of mass with the average $1/p_T^2$ of the two muons, before and after the scaling of $\cot \theta$ given in Equation 3.3. Fitting a line and extrapolating from $\langle 1/p_T^2 \rangle = 0.14 (\text{GeV}/c)^{-2}$ to $\langle 1/p_T^2 \rangle = 0$ gives the systematic uncertainty due to non-linearity. To be conservative, the non-linearity measured before scaling by $\cot \theta$ is used. The extrapolation yields an uncertainty of $0.9 \text{ MeV}/c^2$ when expressed as an uncertainty on the J/ψ mass.

The uncorrected measured value for the J/ψ mass, extracted by fitting the data in Figure 3.3 (see Section 3.3) and applying energy-loss and

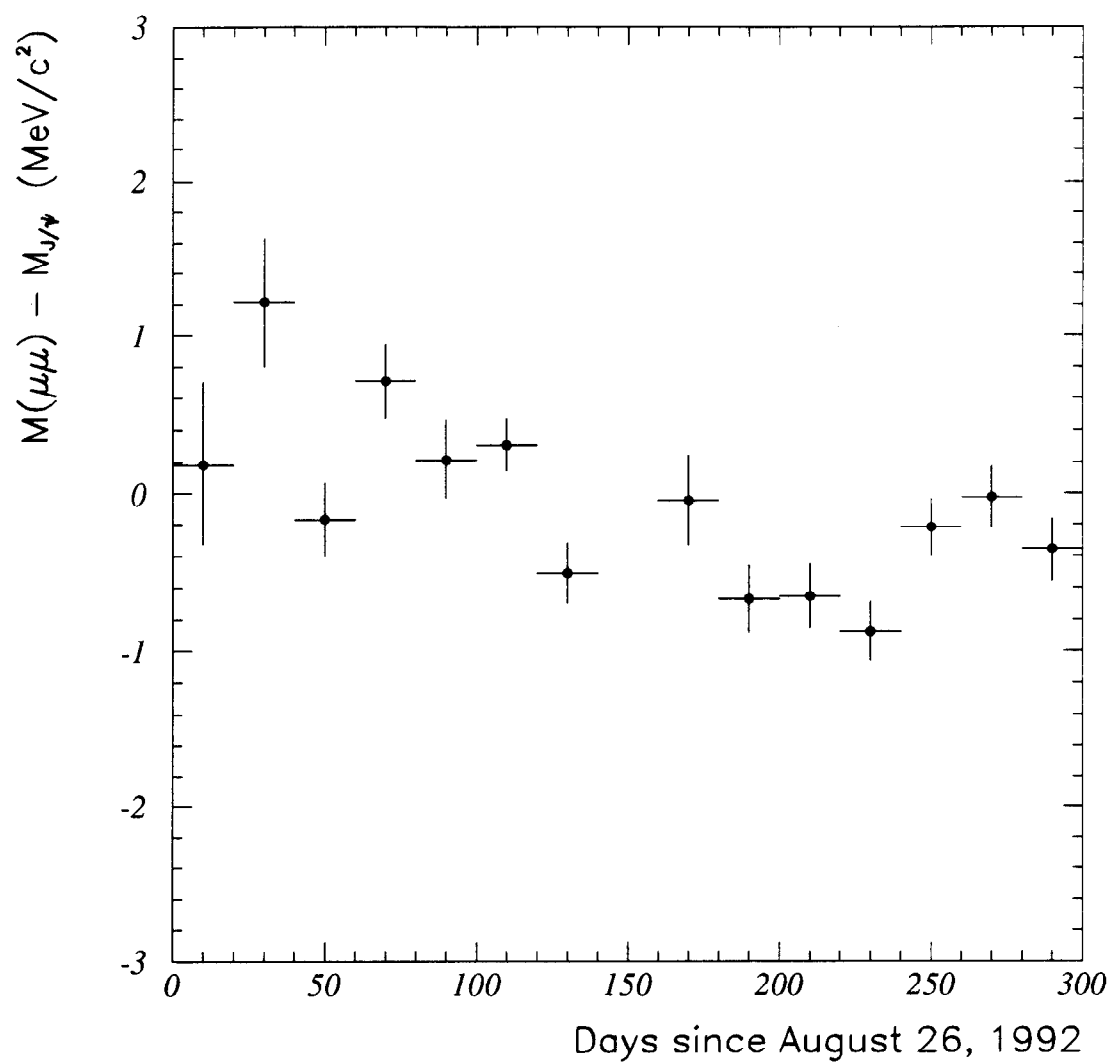


Figure 3.6: Variation of the measured J/ψ mass with time.

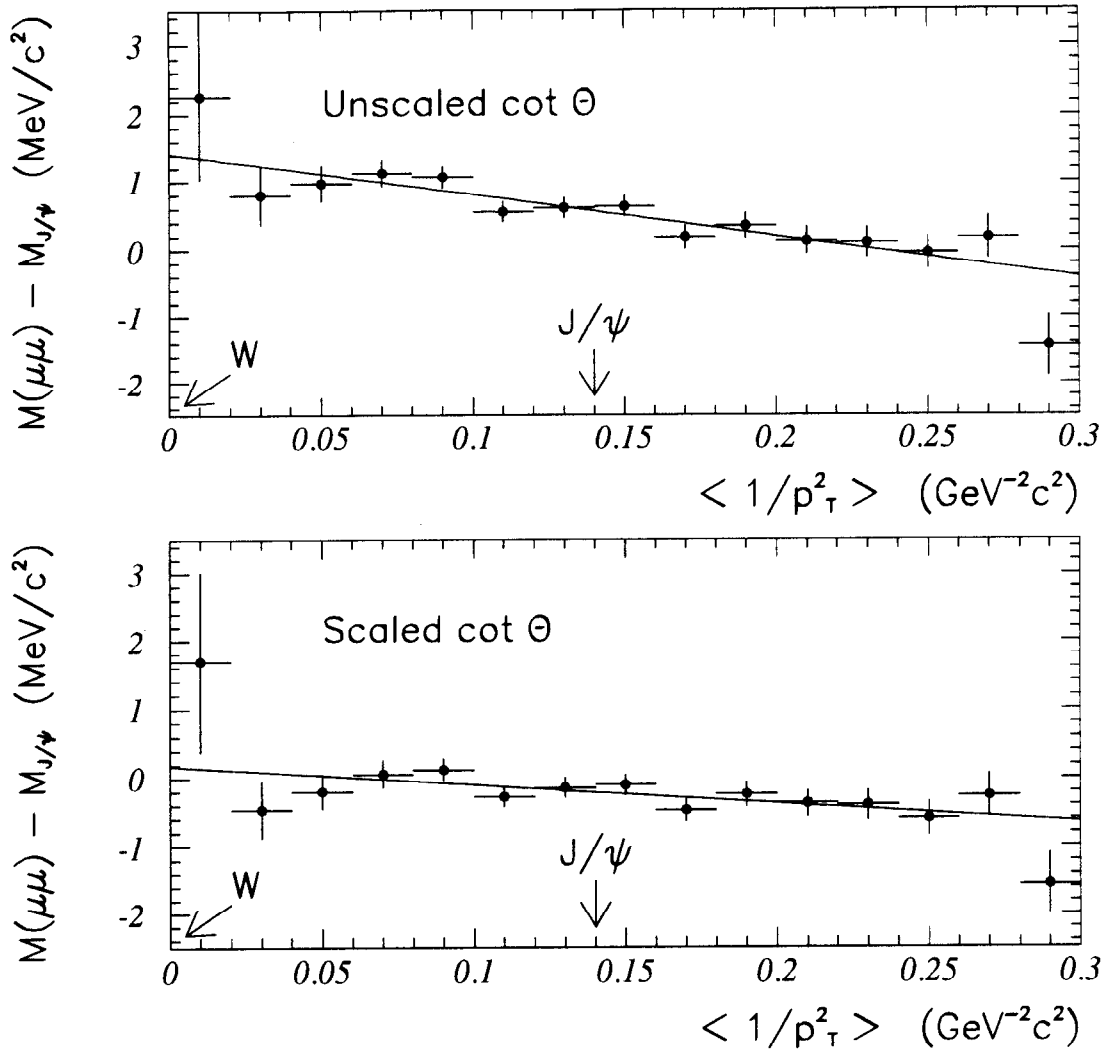


Figure 3.7: Variation of the measured J/ψ mass with the average of $1/p_T^2$ for the two muons. The leptons from W decays would lie in the first bin of this plot ($0.001 \text{ (GeV/c)}^{-2}$). The average for J/ψ decays is $0.14 \text{ (GeV/c)}^{-2}$. The upper plot is before the $\cot \theta$ scaling; the lower plot is after. The slope in the lower plot is a factor of two smaller.

Resonance	Corrected Mass (MeV/c ²)	World-Average Mass (MeV/c ²)
$\Upsilon(1S) \rightarrow \mu\mu$	$9460 \pm 2 \pm 6$	9460.4 ± 0.2
$\Upsilon(2S) \rightarrow \mu\mu$	$10029 \pm 5 \pm 6$	10023.3 ± 0.3
$\Upsilon(3S) \rightarrow \mu\mu$	$10334 \pm 8 \pm 6$	10355.3 ± 0.5
$Z \rightarrow \mu\mu$	$91020 \pm 210 \pm 55$	91187 ± 7

Table 3.2: Measured masses of the $\Upsilon \rightarrow \mu\mu$ and $Z \rightarrow \mu\mu$ resonances compared to the published values [34]. The first uncertainty on the corrected value is from statistics. The second is the systematic uncertainty from the momentum scale.

radiative corrections, is 3097.3 ± 1.6 MeV/c². The momentum scale is corrected by a factor of 0.99984 ± 0.00058 for the J/ψ mass to agree with the world average of 3096.88 ± 0.04 MeV/c² [34], where the uncertainty on the correction factor includes the term accounting for the extrapolation to the W mass. This corresponds to a correction of -11 ± 50 MeV/c² at the W mass.

3.4 Checks

The mass peaks of the first three Υ resonances are shown in Figure 3.8. These check the CTC momentum scale using pairs of tracks with larger opening angles than in $J/\psi \rightarrow \mu\mu$ decays. The measured mass values, after the absolute scale determination and a QED radiation correction of $+3 \pm 1$ MeV/c², are shown in Table 3.2. The agreement for the 1S and 2S masses is good; the value for the 3S peak shows a marginal discrepancy. Note that the 3S peak area is dominated by background.

The mass of the Z boson measured in $Z \rightarrow \mu\mu$ decays checks the momentum scale using tracks with curvatures comparable to those used to measure the W mass. The measurement is limited by the finite statistics in the peak. The measurement, described in detail in Section 4, includes the

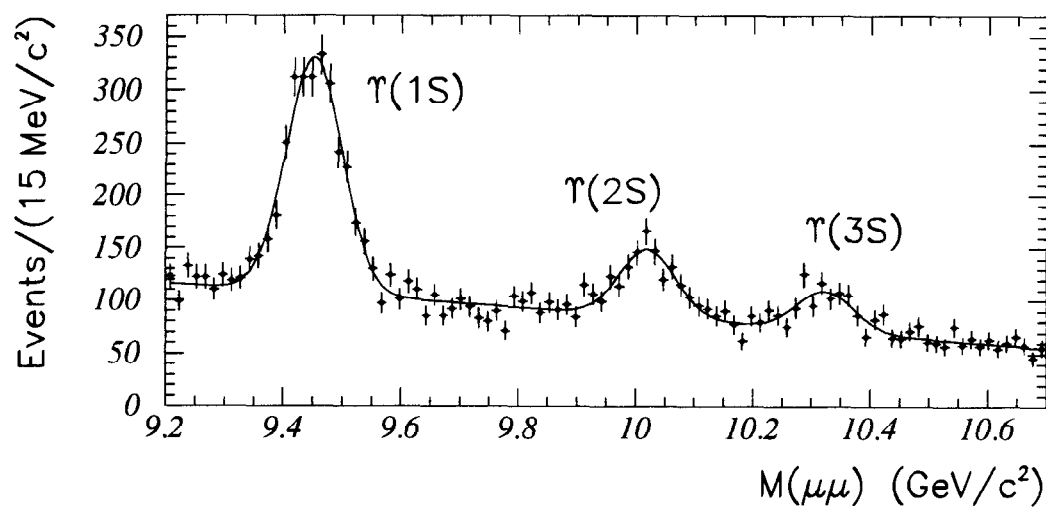


Figure 3.8: The dimuon mass spectrum near the Υ mass. The fits are Gaussians with a quadratic background.

effects of Drell-Yan interference, radiative decays ($Z \rightarrow \mu\mu\gamma$) and the detector resolutions discussed in Section 7. The measured value, $M_Z = 91.02 \pm 0.21$ (stat.) ± 0.07 (syst.) GeV/c², is in good agreement with the LEP result of $M_Z = 91.187 \pm 0.007$ GeV/c² [34]. The tracking resolution is extracted simultaneously with the momentum scale; the result is given in the following section.

3.5 Summary

The absolute momentum scale is determined by normalizing the measured J/ψ mass to the world-average mass. The momentum scale needs to be corrected by a factor of 0.99984 ± 0.00058 . A 50 MeV/c² systematic uncertainty in the W mass measurement is ascribed to the procedure. The possibility of remaining misalignments adds a 15 MeV/c² uncertainty to the W mass measurement.